Molecular Catalysis 451 (2018) 153–160

Contents lists available at ScienceDirect

Molecular Catalysis

journal homepage: www.elsevier.com/locate/mcat

Cubic Mn_2O_3 nanoparticles on carbon as bifunctional electrocatalyst for oxygen reduction and oxygen evolution reactions

Kumar Kashyap Hazarika, Chiranjita Goswami, Himadri Saikia, Biraj Jyoti Borah, Pankaj Bharali*

Department of Chemical Sciences, Tezpur University, Napaam 784 028, Assam, India

ARTICLE INFO

Article history:
Received 31 August 2017
Received in revised form 6 December 2017
Accepted 11 December 2017
Available online 24 December 2017

Keywords:
Mn_2O_3/C
Electrocatalyst
Oxygen reduction
Oxygen evolution reactions

ABSTRACT

Transition metal oxides are most promising non-platinum catalysts for oxygen reduction (ORR) and oxygen evolution reactions (OER) in renewable-energy technologies. Among transition metal oxides, Mn oxides are very active for both ORR and OER and can act as a bifunctional catalyst. But due to their poor electronic conductivity, carbon materials are used as supports or mixed with other metal oxides to increase their conductivity that assistances in electrochemical applications. Herein, a highly active mesoporous cubic material consisting of Mn_2O_3 nanoparticles grown on carbon (Vulcan XC-72 R) as a high performance bifunctional catalyst for both ORR and OER have been synthesized. The synthesized Mn_2O_3/C has been characterized by various structural analyses. The Mn_2O_3/C material exhibits much better ORR activity compared to the commercially available Pt/C and Pd/C in alkaline media. The same material is also active for OER, making it a bifunctional electrocatalyst for both the reactions. Consequently, Mn_2O_3/C is quite stable up to 1000 cycles displaying its better stability. The reaction mechanism follows a 4-electron pathway for ORR. The superior electrocatalytic presentation mainly arises due to the better synergistic coupling effect of carbon and Mn_2O_3.

1. Introduction

The world's ever-growing energy demand combined with the crisis of natural resources inspired the researchers towards extensive exploration of sustainable and renewable energy sources [1]. To overcome these shortcomings, alternative energy storage and conversion devices such as, metal air batteries, fuel cells and water splitting systems have been widely employed as efficient and clean energy sources [2]. Fuel cells are considered to be superior energy converters capable of converting chemical energy of fuels (e.g. hydrogen, methanol, ethanol, etc.) into electrical energy [3]. Among different types of the existing fuel cells, proton exchange membrane fuel cells (PEMFCs) have attracted enormous attention owing to its advantages such as low operation temperature, high energy density, high energy conversion efficiency and more eco-friendly and find wide application in transportation, portables and stationary devices [4]. Similarly, a metal-air battery, characterized by an open cell structure also produces and stores energy via a redox reaction between metal and oxygen in air [5]. However, for worldwide commercialization of these applications in terms of cost, efficiency and longevity, high performance oxygen electrodes are needed [6]. One of the most important reactions that take place in the cathode of fuels cells as well as metal air batteries is the oxygen reduction reaction (ORR) [7,8]. Moreover, oxygen evolution reaction (OER) that generates oxygen during water oxidation is also of great interest due to its significance in the energy conversion devices [9,10]. Both the reactions i.e. ORR and OER depends extremely on the catalyst as well as the electrolyte used and proceed via a four electron reaction pathway involving various intermediates and suitable mechanisms [11]. One of the key drawbacks of both the fuel cells and the metal-air batteries, which lead to loss of cell efficiency, is the sluggish kinetics of oxygen reduction reaction (ORR) and oxygen evolution reaction (OER) that takes place at the cathode and anode of these electrochemical devices [12]. Thus, developing desirable nanocatalysts to overcome the sluggish kinetics of ORR and OER is one of the most demanding tasks [13]. In general, state-of-the-art platinum/carbon (Pt/C) catalyst or platinum based materials are considered to be the best catalyst for ORR and OER in both alkaline and acidic medium due to its excellent electrocatalytic activity [14–16]. However, the high cost, scarcity and low durability prevent its extensive commercial applications. Therefore, much effort has been given towards exploration of cost effective, durable and highly abundant alternative electrocatalysts

* Corresponding author.
E-mail addresses: pankajb@tezu.ernet.in, pbharali@yahoo.com (P. Bharali).

https://doi.org/10.1016/j.mcat.2017.12.012
2468-8231/

with comparable or even higher catalytic performance than that of platinum-based electrocatalysts [17–19].

Replacing platinum with inexpensive metals, developing metal free electrocatalysts or transition metal oxide – based electrocatalysts are ideal approaches to reduce the cost of the electrocatalysts [20,21]. Transition metal oxide (Metal = Ir, Mn, Fe, Co etc) based electrocatalysts have been emerged as an inexpensive alternatives to precious Pt-based materials with outstanding ORR performance [22,23]. Experimental and theoretical reports have shown that transition metal oxides based electrocatalysts act as very suitable electrode material in various electrochemical devices [24]. Recently, manganese oxides (MnO_x) have drawn enormous attention as an appealing ORR catalyst in alkaline medium owing to its high stability, availability, low cost, variable oxidation states and effective catalytic properties [25,26]. Such catalysts with versatile crystallographic structures include MnO, MnO_2, Mn_2O_3, Mn_3O_4 has the potential to replace the expensive benchmarked Pt/C catalysts [27]. The catalytic activity of these oxides is morphology and stoichiometry dependent [28].

Metal catalysts sometimes undergo agglomeration, dissolution and sintering during fuel cell reactions which results in diminishing catalytic activity and stability [29]. Hence, for proper dispersion and to prevent agglomeration the use of an ideal support is very essential [30]. Carbon-based materials have been widely used as catalyst supports in many reactions such as chemical and enzymatic biomass transformation reactions, fuel cell reactions, metal air batteries etc. due to its high specific surface areas, high chemical resistivity, high porosity, superior mechanical strength, excellent electron conductivity and relative chemical inertness [31,32]. The reason behind wide use of carbon-based materials as catalyst supports is the ease of its fabrication in different physical forms and shape. In case of precious metals (like Pt and Pd), the use of graphene and carbon nanotubes (CNTs) as supports is more as compared to other carbon-based supports to improve ORR activity and stability [33,34]. Carbon based materials not only act as active supports but also enhances the poor electronic activity of the transition metal oxide – based electrocatalysts [35]. Thus, the combination of transition metals with carbon support turned out to be promising electrocatalysts that could remarkably increases the catalytic activity and durability owing to their synergistic effects [36].

Herein, we have obtained cubic-Mn_2O_3 nanomaterials supported on Vulcan XC-72 R carbon electrocatalyst via hydrothermal method at 120 °C to investigate its bifunctional electrocatalytic activity towards ORR and OER. The synthesized nanoparticle was found to show high electrocatalytic activities, enhanced mass activity and superior stability in alkaline media as compared to the commercially available Pt/C and Pd/C catalyst. Thus the present work highlights an improved strategy for enhancing the catalytic activity of Mn-oxide nanoparticles toward ORR and OER.

2. Experimental section

2.1. Materials

The chemicals used in this work were manganese chloride tetrahydrate ($MnCl_2{\cdot}4H_2O$), urea and Vulcan XC-72 R carbon black. All the chemicals used were of analytical reagent grade and used as received without further purification. Urea and $MnCl_2{\cdot}H_2O$ were purchased from MERCK specialties Pvt. Ltd. (Mumbai, India). Vulcan XC-72 R carbon black was obtained from Cabot Corporation.

2.2. Synthesis of Mn_2O_3/C nanoparticles

Typically, 0.647 g of $MnCl_2{\cdot}4H_2O$ was dissolved in 40 mL of distilled water. Subsequently, 40 mL of 2.40 g urea was added drop wise to the freshly prepared solution from a burette and stirred for 30 min. The resulting solution is transferred to a 150 mL teflon-lined stainless steel autoclave which was then kept in an oven maintained at a temperature of 120 °C for 6 h. Finally, it was allowed to cool for 15 h then washed, centrifuged with distilled water and with absolute alcohol and dried at 50 °C. The precursor was then calcined in a muffle furnace at 450 °C for 4 h. Again Mn_2O_3/C was prepared by mixing 0.060 g Mn_2O_3 with Vulcan XC-72 R carbon powder in 20% weight ratio, ground for 30 min in an agate mortar and the mixture was ultrasonicated with ethanol (as a solvent) for 30 min. The mixture was allowed to first air dry and then kept in an oven at a temperature of 50 °C.

2.3. Characterization

TGA curve was obtained on a thermal analyser (Model TGA-50, Shimadzu) instrument. The samples were heated from ambient temperature to 600 °C under N_2 flow at heating rate of 10 °C min^{-1}. X-ray diffraction was used to investigate the bulk phases present in the samples. The powder X-ray diffraction patterns were recorded on D8 FOCUS (BRUKER AXS, GERMANY) instrument. The intensity data were collected over 2θ range of 10–80°. Infra-red spectra were measured in a FTIR spectrophotometer, Model Nicolet Impact I-410. Measurements were performed by pelletizing the samples with KBr in the mid-IR region. The scanning electron microscope (SEM) uses a focused beam of high-energy electrons to generate a variety of signals at the surface of solid specimens. The signals that derive from electron-sample interactions reveal information about the sample including external morphology (texture), chemical composition, and crystalline structure and orientation of materials making up the sample. To study the surface topography, SEM analysis were carried out with JEOL, JSM model 6390 LV scanning electron microscopes, operating at an accelerating voltage of 15 kV. The TEM investigations were carried out on TECNAI G^2 20 S-TWIN (FEI COMPANY, USA) having resolution of 2.4 Å equipped with a slow scan CCD camera and an accelerating voltage of 200 kV. Raman spectroscopy has been extensively employed to discriminate between different structures on oxide surfaces. Raman spectra were collected using 514 nm laser source in a RENISHAW, UK Raman spectrometer under ambient conditions. BET surface area was determined by N_2 adsorption-desorption using a Quantachrome instrument (Model: NOVA 1000e). The pore size and pore volume were determined following Barrett-Joyner-Halenda (BJH) method in the same instrument. The XPS studies were performed using a Thermo K-Alpha XPS equipped with an Al Kα radiation (1486.6 eV) X-ray source at a pressure < 10^{-7} Torr and an electron take-off angle (angle between electron emission direction and surface plane) of 90°. A survey scan was performed using pass energy of 200 eV to determine possible contaminants. The binding energies of the samples were charge-corrected with respect to the adventitious carbon (C 1s) peak at 284.6 eV.

2.4. Fabrication of electrodes and electrochemical measurements

All the measurements were performed under identical conditions. The working electrode was prepared by dispersing 5 mg of Mn_2O_3/C in 0.5 mL of ethanol-water and 0.5 mL nafion solution (0.5 wt.%). To get a homogeneous suspension the mixture was ultrasonicated for 30 min. Then 6 μL was loaded on the surface of the glassy carbon electrode with a diameter of 3 mm and dried slowly in N_2 atmosphere at 35°C in a vacuum oven to achieve a uniform surface. Finally a Pt/C and Pd/C catlalysts were used as comparison and fabricated exactly as the Mn_2O_3/C. Electrochemical measurements were performed in 0.1 M KOH electrolyte in a standard three electrode cell at room temperature using an Autolab PGSTAT 204 potentiostat/galvanostat (Metrohm, Autolab,

The Netherlands). The cell consists of a Pt wire counter electrode, Ag/AgCl reference electrode and the fabricated working electrode. All the electrochemical tests were carried out in a solution of O_2- or N_2- saturated 0.1 M KOH solution. A flow of O_2 was maintained in order to ensure its continued O_2 saturation during the recording of electrochemical measurements over the electrolyte (0.1 M KOH). Using a glassy carbon RDE cyclic voltammograms (CVs) and linear sweep voltammograms (LSVs) were recorded. The scan rate of CVs and LSVs were kept at 50 mVs^{-1} and 10 mVs^{-1}, respectively. To confirm the reversibility of the catalyst LSVs were performed at forward and backward currents. The stability experiments were further measured by cycling Mn_2O_3/C 1000 times. RDE measurements were performed at different rotating rate of 400, 900, 1600, 2500 and 3600 rpm. The overall electron transfer numbers per oxygen molecule involved can be calculated from the slopes of Koutecky-Levich (K-L) equation in a typical ORR process.

$$\frac{1}{j} == \frac{1}{j_k} + \frac{1}{B\omega^{0.5}} \quad (1)$$

$$B = 0.62\,nF(Do_2)^{2/3}\nu^{-1/6}Co_2 \quad (2)$$

Where j is the current density, j_k is the kinetic current density in amperes at a constant potential, ω is the rotating rate of the electrode in rpm and B is the slope which could be obtained from the Koutecky-Levich plots. F is the Faraday constant (96500C mol^{-1}), Do_2 is the diffusion co-efficient of O_2 in 0.1 M KOH (2.0×10^{-5} $cm^2 s^{-1}$), ν is the kinetic viscosity (0.01 cm^2 s^{-1}), Co_2 is the bulk concentration of O_2 (1.2×10^{-6} mol cm^{-3}) and the value of 'n' represents the number of transferred electrons transferred per oxygen molecule in the ORR process.

3. Results and discussion

3.1. Structural analysis of Mn_2O_3/C

The Mn_2O_3/C was characterized by various analytical techniques and the electrochemical measurements were studied. XRD was performed to investigate the phase structure of the synthesized Mn-oxide. Fig. 1a presents the XRD profiles of Mn_2O_3/C, standard Mn_2O_3. In Fig. 1a, diffraction peaks are observed at 2θ = 32.9, 55.1, 23.1, 38.2, 65.7, 49.3 and 45.1° which could be assigned to (222), (440), (211), (400), (622), (431) and (332) reflections, respectively which are in good agreement with the standard Mn_2O_3/Cubic phase (JCPDS card no. 71-0636) and the most intense peak at 2θ of 32.9° corresponding to the d-spacing of 0.27 nm. The XRD profile of Vulcan XC-72 R carbon powder is presented in Fig. S1 in the Electronic Supplementary Material.

The phases of Mn_2O_3/C were further confirmed by Raman spectroscopy. Raman spectroscopy is a useful non-destructive tool to distinguish between disordered and ordered carbon structures. The typical Raman spectra of Mn_2O_3/C is shown in Fig. 1b, where the peaks of Raman spectrum of Mn_2O_3/C at 1356 and 1625 cm^{-1} can be attributed to D (due to the presence of disorder in sp^2-hybridized carbon systems) and G (arises from stretching of C—C bond) bands of carbonaceous materials [24,37]. No characteristic peak was observed for Mn_2O_3. In Fig. 1c the FT-IR spectra of the Mn_2O_3/C is presented, the Mn_2O_3 after annealing show two distinct bands in the lower mid-infrared 500–700 cm^{-1} range originating from the stretching vibrations of the metal-oxygen bond. Two very strong peaks at 565 cm^{-1} and 669 cm^{-1} observed are characteristics of OB_3 (B – Mn^{3+} in an octahedral site), the band near 3423 cm^{-1} is attributed to O—H stretching due to physisorbed water molecules [38,39]. Fig. 1d presents the TGA curve of Mn-oxide precursor before annealing. From the figure it is observed that a substantial mass loss of ~33% occur in the temperature ranges of ambient temperature to 450 °C. This substantial mass loss may be attributed to the dehydration and dehydroxylation of the sample, decomposition of the organic residues and pyrolysis of counter anions into gases [39]. After 450 °C no major weight loss is observed. Accordingly we have employed 450 °C as optimum temperature for annealing of as synthesized Mn-oxide precursor.

The microstructure and morphology of the as-synthesized material was characterized by scanning electron microscopy (SEM). From the SEM images of the as-synthesized Mn-oxide precursor at two different resolutions it is observed that it forms a cube like structure. After the preparation of the carbon supported Mn-oxide i.e, Mn_2O_3/C the morphology of the material was changed and shows some extent of aggregation and the particles are uniformly anchored on the surface of the carbon (Fig. S2, Electronic Supplementary Material).

To further investigate the structure and morphology of the sample TEM analyses of the Mn_2O_3/C are accomplished. The TEM images confirm the homogeneous distribution of the nanosized Mn_2O_3 particles on the carbon support (Fig. 2). The size and the distribution of the particles were determined and found that most of the particles are of spherical morphology and fall in the range of 6–8 nm (inset of Fig. 2a). The selected area diffraction (SAED) pattern confirms that the mesoporous walls are composed of crystalline Mn_2O_3/C nanoparticles (inset of Fig. 2b). In the SAED pattern the well-defined cricoid diffraction rings are observed which clearly signify the polycrystallinity of the sample. The HRTEM micrographs exhibits clear lattice fringe as shown in the inset of Fig. 2c, the lattice spacing is found to be 0.27 nm which corresponds to the inter-planner distance of (222) crystalline plane of Mn_2O_3/C NPs.

X-ray photoelectron spectra (XPS) was recorded to investigate the chemical bonding states and composition of the synthesized material. From the spectrum the existence of manganese, oxygen can be observed shown in Fig. 3a, b. As shown in Fig. 3a, two peaks at 641.4 and 653.2 eV are observed in the XP spectra for the Mn 2p of the Mn_2O_3, corresponding to the Mn $2p_{3/2}$ and Mn $2p_{1/2}$ spin-orbit states of Mn_2O_3 with a spin energy gap of 11.8 eV which further verifies the presence of Mn_2O_3 [24,39,40]. Mn is preferentially present in the Mn^{3+} state on the surface of the catalyst. The O 1 s electron emission is bi-dispersed as shown in Fig. 3b. The peak at 529.6 eV originates from the low-energy electrons of O^{2-} species, whereas the high-energy peak at 531.1 eV arise from OH^- species [39,41]. The contributions of other charged oxygen species could be the reason for the broadening of the O^{2-} peak [39]

N_2 adsorption/desorption isotherm was measured to explore the pore structure of the Mn_2O_3/C at −196 °C. As depicted in Fig. 3c, the isotherm of the Mn_2O_3/C displays the typical type-IV with a distinctive H3 hysteresis loop at relative pressure (P/P_o) from 0 to 1.0 [41]. The BET surface area of Mn_2O_3/C was estimated to be 116 m^2/g. The mean pore size (inset Fig. 3c) is 3.6 nm for Mn_2O_3/C composite. The high surface area of the Mn_2O_3/C is expected to facilitate the molecular transport and oxygen adsorption during ORR/OER process.

3.2. Electrochemical measurements

The catalytic activity of the Mn_2O_3/C nanocomposites and Mn_2O_3 for ORR was characterized by electrochemical methods. Fig. 4a,d illustrates the cyclic voltamograms (CV) of the synthesized samples in O_2/N_2 saturated 0.1 M KOH on a glassy carbon (GC) electrode at a scan rate of 50 mVs^{-1}. As shown in Fig. 4a,d, one obvious ORR characteristic peak centred at −0.25 V and at −0.45 V in the range 0.2–−0.8 V vs. Ag/AgCl is observed suggesting the electrochemical reduction of oxygen over Mn_2O_3/C and Mn_2O_3. A better reduction peak is observed in O_2 saturated KOH solution compared to that of N_2 [42]. This suggests enhanced electrocatalytic activity of Mn_2O_3/C nanocomposites towards ORR in alkaline medium.

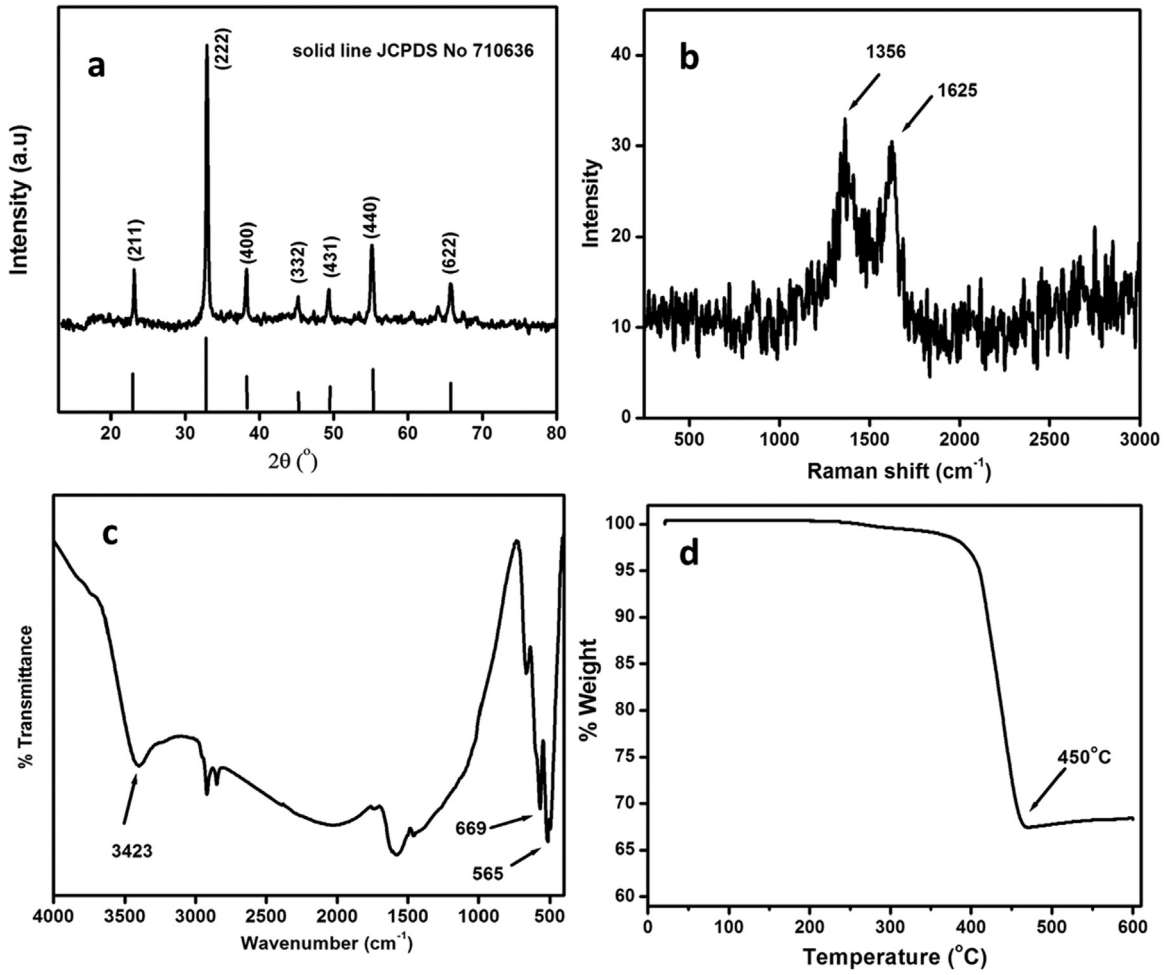

Fig. 1. (a, b) XRD profile and Raman spectra of Mn_2O_3/C, (c) FT-IR spectra of Mn_2O_3, (d) TGA profile of as synthesized Mn_2O_3 precursor.

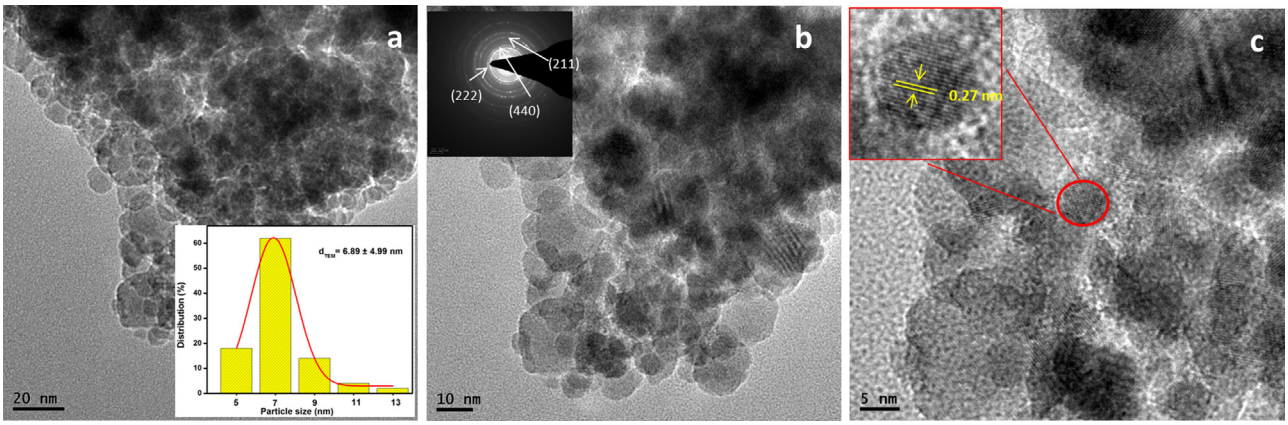

Fig. 2. (a,b) TEM and (c) HRTEM images of Mn_2O_3/C; inset (a) corresponding particle size distribution, inset (b) corresponding SAED pattern and inset (c) single Mn_2O_3 crystal with lattice fringe.

Further investigation of the electrocatalytic properties of the Mn_2O_3/C nanocomposites and Mn_2O_3 towards ORR were performed by rotating disc electrode (RDE) measurements in O_2 saturated 0.1 M KOH. Fig. 4b,e shows the LSV curves of the samples at different rotating speed ranging from 400 to 3600. It has been observed that with increase in the rotation speed of the electrode, the current density of ORR also increases which can be attributed to the high diffusion rates at higher rotating speeds [1,2]. The Mn_2O_3/C displays an onset potential of −0.08 V vs. Ag/AgCl in the LSVs, which is more positive and larger ORR current density compared to Pt/C and Pd/C catalysts. However, only Mn_2O_3 displays an onset potential of −0.20 V which is less positive and shows smaller ORR current density compared to Mn_2O_3/C and both Pt/C and Pd/C catalysts. This demarcates the synergistic influence of Mn_2O_3 and C in hybrid

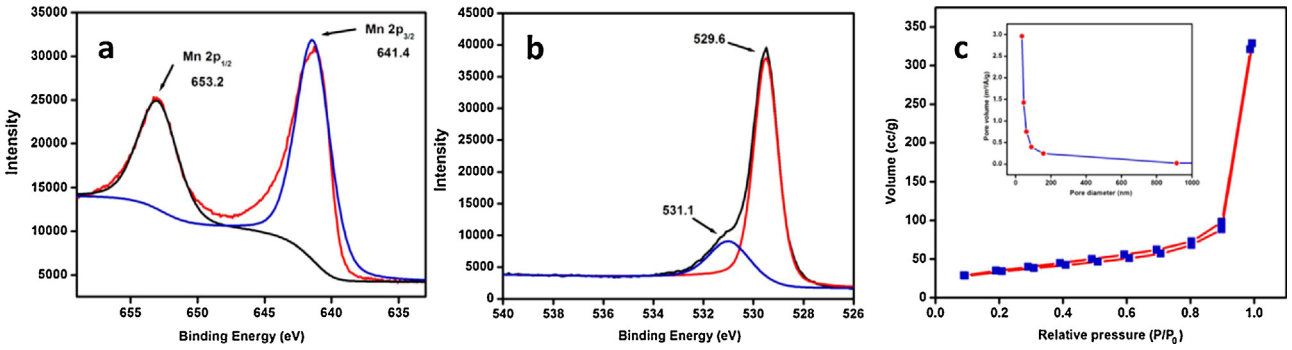

Fig. 3. XP spectra of Mn_2O_3; core level XP spectrum of (a) Mn 2p, (b) O 1 s and (c) N_2 adsorption/desorption isotherm and the pore size distribution curve (inset) of Mn_2O_3/C.

Mn_2O_3/C over only Mn_2O_3. The high electrocatalytic activity relates to the fact that the Mn (III), which is electronically degenerate inclines to unveil higher specific activities towards ORR and OER [40]. Also the longer bond lengths of Mn–O, the effect of using carbon material as a support and the Mn (III) moiety are supposed to contribute to the higher catalytic activity [26,40].

The total number of transferred electron 'n' in the ORR process can be calculated from the slope of the K-L plots. The parallel fitting lines and good linearity of the K-L plots at different potentials suggest (Fig. 4c,f) first-order reaction kinetics towards the concentration of dissolved oxygen and similar electron transfer numbers for ORR at different potentials [43]. The average electron transferred for the ORR over Mn_2O_3/C was calculated to be ≈4.1 from −0.4 to −0.55 V vs. Ag/AgCl which is very close to 4.0, whereas it was only ≈1.2 over Mn_2O_3. The average electron transferred for the ORR at different potentials is shown in Fig. 4g. The electron transferred number (n) obtained from the Koutecky–Levich plots based on the RDE measurements was consistent with RDE result, indicating that the ORR mechanism proceeds mainly through the four electron ($4e^-$) pathway ($O_2 + 2H_2O + 4e^- = 4OH^-$) in case of Mn_2O_3/C. The cyclic voltammogram of Vulcan XC-72 R carbon powder on glassy carbon electrode in N_2 and O_2-saturated 0.1 M KOH solution, ORR polarization curves at different rotation rates and Koutecky-Levich plots of j^{-1} vs. $\omega^{-1/2}$ at different potentials are presented in Fig. S3 – S5, Electronic Supplementary Material. This shows that Vulcan XC-72 R carbon powder itself is inferior in its ORR activity.

In alkaline solution, O_2 is reduced to form OH^- by a $4e^-$ process [1]. In addition to ORR, we reviewed the bi-functionality of the Mn_2O_3/C material by testing the OER performance in 0.1 M KOH solution as well. In the last few years, extensive work have been made to develop proficient electrocatalyst for OER as it is play a dynamic role in several energy conversion and fuel cell applications. Fig. 5a shows the combined OER-ORR performance of the cubic Mn_2O_3/C compared with the commercially available (20 wt%) Pt/C and Pd/C in alkaline media (0.1 M KOH) using LSV in the potential booth of 0.2 V to 0.8 V vs. Ag/AgCl. The Mn_2O_3/C displayed high current density (3.1 $mAcm^{-2}$) and earliest onset potential (0.55 V) than that of Pd/C but slightly lower than Pt/C, which signifies the high electrocatalytic activity towards OER.

Additionally, in Fig. 5a, the LSV plots for Mn_2O_3/C, (20 wt%) commercial Pt/C and Pd/C at 1600 rpm is compared from which it can be noted that the synthesized Mn_2O_3/C catalyst displays more positive ORR onset potential and lower current density compared to that of the (20 wt%) commercial Pt/C and Pd/C. Mn_2O_3/C shows ORR onset potential of −0.08 V which is much more positive than that of Pd/C (−0.15 V) and Pt/C (−0.11 V). The above results revealed that Mn_2O_3/C exhibited much higher electrocatalytic activity toward OER and ORR. There are various intermediates that can be form under distinctive ORR conditions which are very difficult to detect, however, ORR tends to follows an associative pathway/mechanism with the formation of superhydroxyl *OOH species which further dissociates to form O and OH by the cleavage of O—O bond [42,44]. It can be believed that for Mn_2O_3/C the dissociation of *OOH, i.e., O—O bond dissociation is more positive. Thus, these outcomes propose that Mn_2O_3/C is an effective bi-functional electrocatalyst toward ORR and OER because of synergistic influence of Mn_2O_3 and carbon interface and preferentially presence of catalytically active Mn^{3+} site on the surface. In the meantime the mass specific activities (j_m) are calculated for the ORR process at various potentials in the range of −0.40 V and −0.55 V for the Mn_2O_3/C catalyst together with the available (20 wt%) commercial Pt/C and Pd/C. Fig. 5b shows the plot of mass specific activities of Mn_2O_3/C, (20 wt%) commercial Pt/C and Pd/C at different potentials. Based upon the calculated value, it should be stated that Mn_2O_3/C, hold almost two times greater mass activity compared to that of commercial Pd/C and slightly better than the commercial Pt/C. Catalyst stability and durability have been considered as key points to evaluate the catalytic performance of an electrocatalyst and also for practical application. We have performed LSV at 1600 rpm after 1000 reaction cycles to study the stability of the Mn_2O_3/C catalyst. As it can be seen from Fig. 5c, that the difference of $\Delta E_{1/2}$ with the initial is quite low suggesting the Mn_2O_3/C catalyst has very high catalytic stability. The above analysis demonstrates that the Mn_2O_3/C possesses high durability and good recycling stability and can be effectively used as cathode catalyst in alkaline fuel cell.

4. Conclusions

In summary, we have demonstrated the superior behaviour of Mn_2O_3/C electrocatalyst as compared to that of the commercial Pt/C and Pd/C for ORR and OER in alkaline medium (0.1 M KOH). The synthesized catalyst was structurally and morphologically characterized by a range of techniques. The Mn_2O_3/C catalyst shows good activity giving 'n' value 4.1 as the number of electron transferred. The mass specific activity of Mn_2O_3/C catalyst is almost two times higher than that of the commercial Pd/C and slightly better than the Pt/C. In addition, the catalyst remains almost stable after 1000 continuous redox cycles confirming an outstanding stability of the catalyst. It is exciting to note that Mn_2O_3/C displays tunable catalytic activity toward OER in alkaline medium. Thus, the present study signifies an excellent bifunctional electrocatalyst for ORR as well as OER in alkaline medium with a favourable onset-potential, electron transfer number (≈4.1), high current density and better durability. Thus the synthesized Mn_2O_3/C as cathode catalyst has great promising applications in alkaline fuel cell.

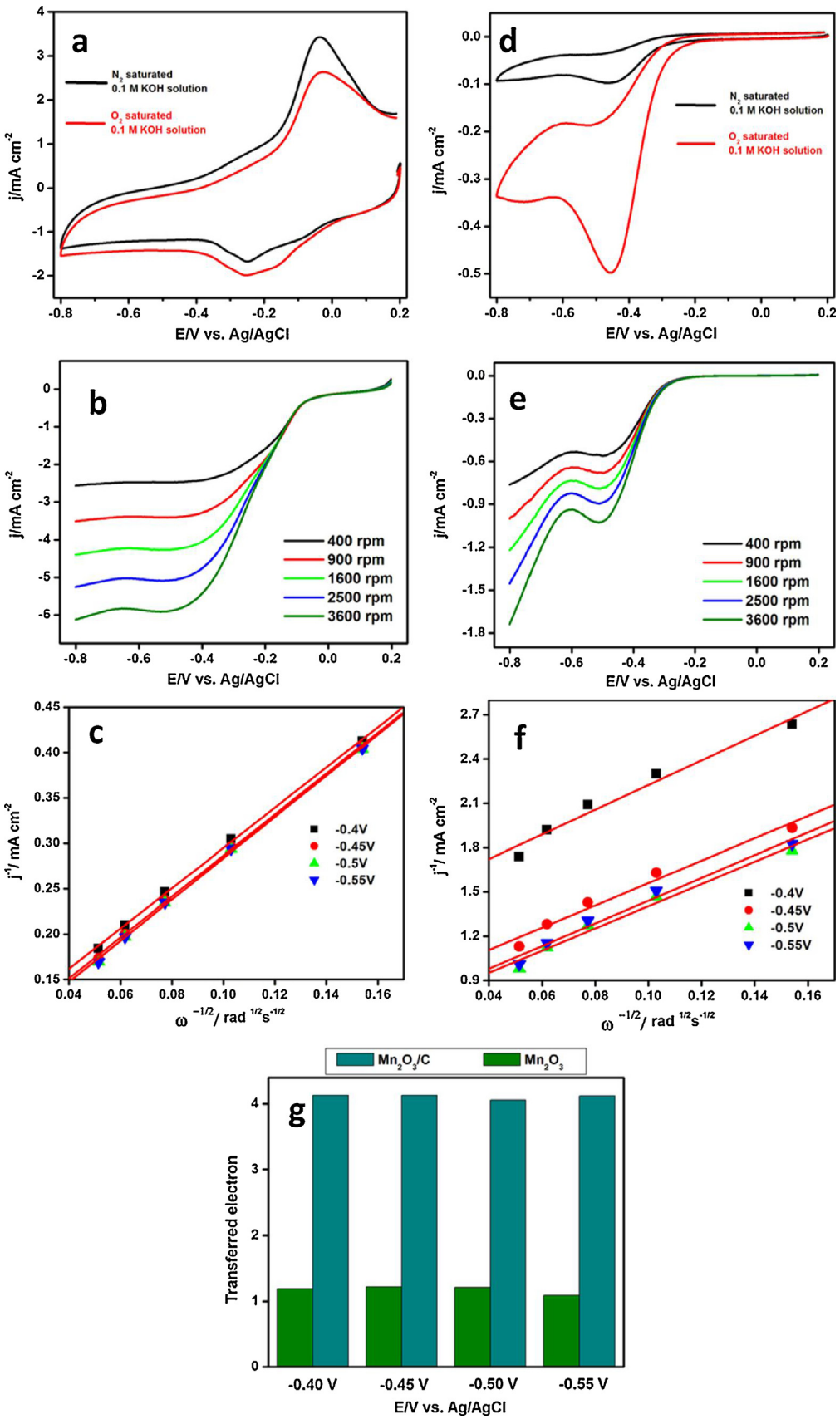

Fig. 4. (a, d) Cyclic voltammogram of Mn_2O_3/C and Mn_2O_3 on glassy carbon electrode in N_2 and O_2-saturated 0.1 M KOH solution; (b, e) ORR polarization curves of Mn_2O_3/C and Mn_2O_3 in O_2 −saturated 0.1 M KOH solution at different rotation rates; (c, f) the Koutecky-Levich plots of j^{-1} vs. $\omega^{-1/2}$ at different potentials for Mn_2O_3/C and Mn_2O_3; (g) Number of electron transferred at different potentials.

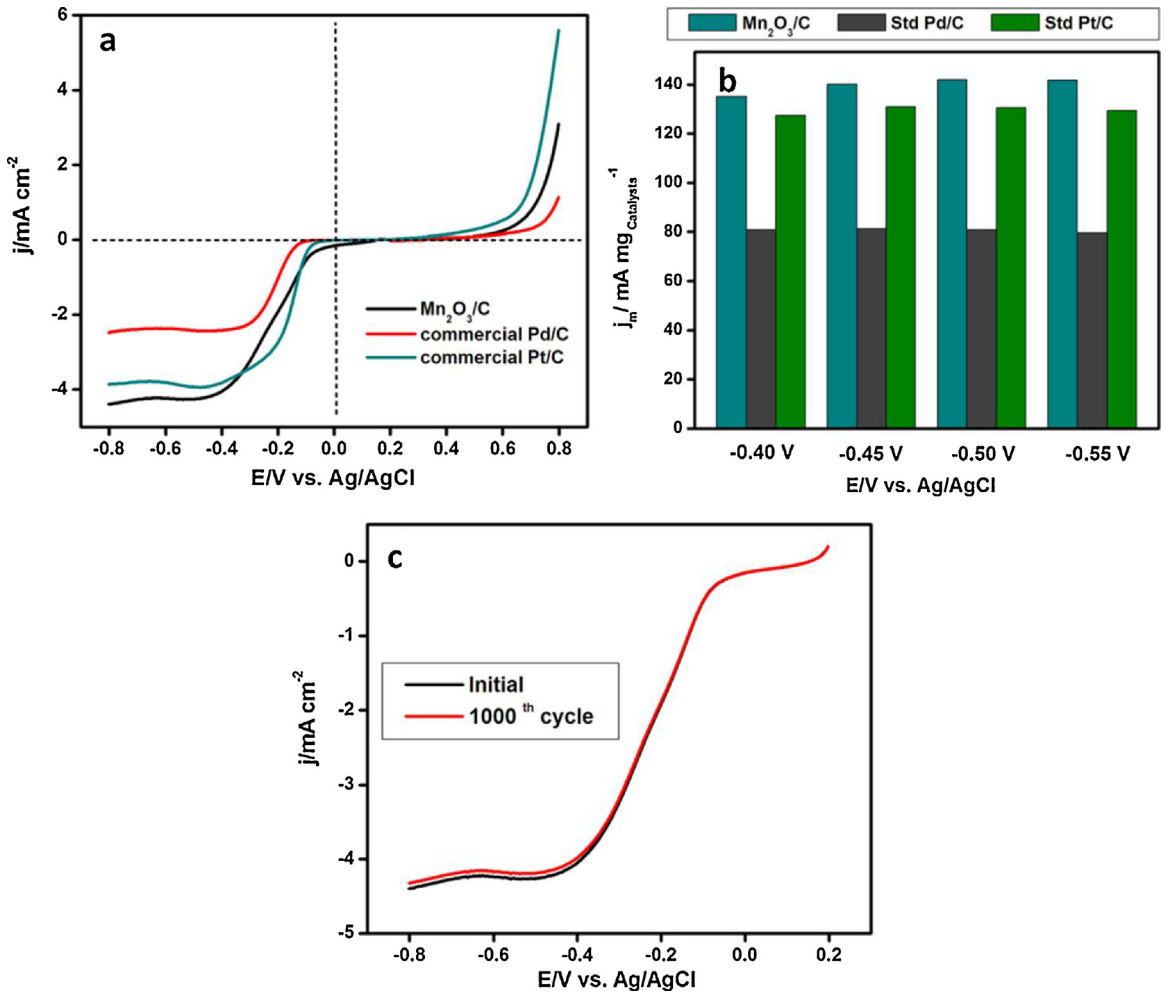

Fig. 5. (a) ORR and OER activities of Mn_2O_3/C, (b) mass specific activities of Mn_2O_3/C at different potentials compared to Pt/C and Pd/C and (c) LSV curve of Mn_2O_3/C after 1000 cycles to check the stability.

Acknowledgments

The authors thank Council of Scientific and Industrial Research (CSIR No: 01(2813)/14/EMR-II), New Delhi and Science and Engineering Research Board (SERB-DST No: SB/FT/CS-048/2014), New Delhi for financial support. SAIC, Tezpur University is acknowledged for instrumental facilities. We thank Prof. S. K. Bhargava and Dr. P. Sudarsanam of RMIT, Australia and RMIT Microscopy and Microanalysis Facility (RMMF) for providing access to XPS analysis used in this study.

Appendix A. Supplementary data

Supplementary data associated with this article can be found, in the online version, at https://doi.org/10.1016/j.mcat.2017.12.012.

References

[1] S. Guo, S. Zhang, S. Sun, Tuning nanoparticles catalysis for the ORR, Angew. Chem. Int. Ed. 52 (2013) 8526–8544.
[2] M. Wang, T. Qian, S. Liu, J. Zhou, C. Yan, Unprecedented activity of bifunctional electrocatalyst for high power density aqueous zinc–air batteries, ACS Appl. Mater. Interfaces 9 (2017) 21216–21224.
[3] Y. Wang, D.-Y.-C. Leung, J. Xuan, H. Wang, A review on unitized regenerative fuel cell technologies, part B: unitized regenerative alkaline fuel cell, solid oxide fuel cell, and microfluidic fuel cell, Renew. Sustain. Energy Rev. 75 (2017) 775–795.
[4] Y.-J. Wang, D.P. Wilkinson, J. Zhang, Noncarbon support materials for polymer electrolyte membrane fuel cell electrocatalysts, Chem. Rev. 111 (2011) 7625–7651.
[5] F. Cheng, J. Chen, Metal–air batteries: from oxygen reduction electrochemistry to cathode catalysts, Chem. Soc. Rev. 41 (2012) 2172–2192.
[6] A. Loh, K. Xu, X. Li, B. Wang, Influence of synthesis parameters on amorphous manganese dioxide catalyst electrocatalytic performance, Electrochim. Acta 245 (2017) 615–624.
[7] J. Chen, N. Zhou, H. Wang, Z. Peng, H. Li, Y. Tang, K. Liu, Synergistically enhanced oxygen reduction activity of MnOx–CeO_2/Ketjenblack composites, Chem. Commun. 51 (2015) 10123–10126.
[8] Q. Tang, L. Jiang, J. Liu, S. Wang, G. Sun, Effect of surface manganese valence of manganese oxides on the activity of the oxygen reduction reaction in alkaline media, ACS Catal. 4 (2014) 457–463.
[9] I.M. Mosa, S. Biswas, Abdelhamid M. El-Sawy, Venkatesh Botu, C. Guild, W. Song, R. Ramprasad, J.F. Rusling, S.L. Suib, Tunable mesoporous manganese oxide for high performance oxygen reduction and evolution reactions, J. Mater. Chem. A 4 (2016) 620–631.
[10] L. Yan, Y. Lin, X. Yu, W. Xu, T. Salas, H. Smallidge, M. Zhou, H. Luo, $La_{0.8}Sr_{0.2}MnO_3$ based perovskite nanoparticles with the a-site deficiency as high performance bifunctional oxygen catalyst in alkaline solution, ACS Appl. Mater. Interfaces 9 (2017) 23820–23827.
[11] W.G. Hardin, J.T. Mefford, D.A. Slanac, B.B. Patel, X. Wang, S. Dai, X. Zhao, R.S. Ruoff, K.P. Johnston, K.J. Stevenson, Tuning the electrocatalytic activity of perovskites through active site variation and support interactions, Chem. Mater. 26 (2014) 3368–3376.
[12] H.-Q. Dong, Y.-Y. Chen, M. Han, S.-L. Li, J. Zhang, J.-S. Li, Y.-Q. Lan, Z.-H. Dai, J.-C. Bao, Synergistic effect of mesoporous Mn_2O_3-supported Pd nanoparticle catalysts for electrocatalytic oxygen reduction reaction with enhanced performance in alkaline medium, J. Mater. Chem. A 2 (2014) 1272–1276.
[13] A.B. Yousaf, M. Imran, N. Uwitonze, A. Zeb, S.J. Zaidi, T.M. Ansari, G. Yasmeen, S. Manzoor, Enhanced electrocatalytic performance of Pt_3Pd_1 alloys supported on CeO_2/C for methanol oxidation and oxygen reduction reactions, J. Phys. Chem. C 121 (2017) 2069–2079.

[14] Y. Liang, H. Wang, J. Zhou, Y. Li, J. Wang, T. Regier, H. Dai, Covalent hybrid of spinel manganese–cobalt oxide and graphene as advanced oxygen reduction electrocatalysts, J. Am. Chem. Soc. 134 (2012) 3517–3523.
[15] Y. Su, H. Chai, Z. Sun, T. Liu, D. Jia, W. Zhou, High-performance manganese nanoparticles on reduced graphene oxide for oxygen reduction reaction, Catal. Lett. 146 (2016) 1019–1026.
[16] S. Liu, C. Deng, L. Yao, H. Zhong, H. Zhang, The key role of metal dopants in nitrogen-doped carbon xerogel for oxygen reduction reactions, J. Power Sources 269 (2014) 225–235.
[17] K. Liu, X. Huang, H. Wang, F. Li, Y. Tang, J. Li, M. Shao, Co_3O_4-CeO_2/C as a highly active electrocatalyst for oxygen reduction reaction in al-air batteries, ACS Appl. Mater. Interfaces 8 (2016) 34422–34430.
[18] F. Cheng, Y. Su, J. Liang, Z. Tao, J. Chen, MnO_2-based nanostructures as catalysts for electrochemical oxygen reduction in alkaline media, Chem. Mater. 22 (2010) 898–905.
[19] K. Mohanraju, P.S. Kirankumar, L. Cindrella, O.J. Kwon, Enhanced electrocatalytic activity of Pt decorated spinals (M_3O_4, M = Mn Fe, Co)/C for oxygen reduction reaction in PEM fuel cell and their evaluation by hydrodynamic techniques, J. Electroanal. Chem. 794 (2017) 164–174.
[20] M. Zhou, H.-L. Wang, S. Guo, Towards high-efficiency nanoelectrocatalysts for oxygen reduction through engineering advanced carbon nanomaterials, Chem. Soc. Rev. 45 (2016) 1273–1307.
[21] Y. Nie, L. Li, Z. Wei, Recent advancements in Pt and Pt-free catalysts for oxygen reduction reaction, Chem. Soc. Rev. 44 (2015) 2168–2201.
[22] O. Luigi, H.A. Alessandro, V. Monteverde, A. Marco, S. Stefania, Influence of different transition metals on the properties of Me–N–C (Me = Fe, Co Cu, Zn) catalysts synthesized using SBA-15 as tubular nano-silica reactor for oxygen reduction reaction, Int. J. Hydrogen Energy 41 (2016) 22570–22588.
[23] O. Hannah, S.V. Devaguptapua, X. Hui, C. Jaephil, W. Gang, Transition metal (Fe, Co, Ni, and Mn) oxides for oxygen reduction and evolution bifunctional catalysts in alkaline media, Nano Today 11 (2016) 601–625.
[24] H. Chai, J. Xu, J. Han, Y. Su, Z. Sun, D. Jia, W. Zhou, Facile single-step synthesis of nitrogen-doped reduced graphene oxide-Mn_3O_4 hybrid functional material for the electrocatalytic reduction of oxygen, J.Colloid Interface Sci. 488 (2017) 251–257.
[25] T.N. Lambert, J.A. Vigil, S.E. White, C.J. Delker, D.J. Davis, M. Kelly, M.T. Brumbach, M.A. Rodriguez, B.S. Swartzentruber, Understanding the effects of cationic dopants on α-MnO_2 oxygen reduction reaction electrocatalysis, J. Phys. Chem. C 121 (2017) 2789–2797.
[26] A.S. Ryabova, A. Bonnefont, P.A. Simonov, T. Dintzer, C. Ulhaq-Bouillet, Y.G. Bogdanova, G.A. Tsirlina, E.R. Savinova, Further insights into the role of carbon in manganese oxide/carbon composites in the oxygen reduction reaction in alkaline media, Electrochim. Acta 246 (2017) 643–653.
[27] R. Miao, J. He, S. Sahoo, Zhu Luo, Wei Zhong, S.-Y. Chen, C. Guild, T. Jafari, B. Dutta, S.A. Cetegen, M. Wang, S.P. Alpay, S.L. Suib, Reduced graphene oxide supported hierarchical flower like manganese oxide as efficient electrocatalysts toward reduction and evolution of oxygen, ACS Catal. 7 (2017) 819–832.
[28] S. Sun, H. Miao, Y. Xue, Q. Wang, S. Li, Z. Liu, Oxygen reduction reaction catalysts of manganese oxide decorated by silver nanoparticles for aluminum-air batteries, Electrochim. Acta 214 (2016) 49–55.
[29] A. Cao, R. Lu, G. Veser, Stabilizing metal nanoparticles for heterogeneous catalysis, Phys. Chem. Chem. Phys. 12 (2010) 13499–13510.
[30] X. Chen, G. Wu, J. Chen, X. Chen, Z. Xie, X. Wang, Synthesis of clean and well-dispersive Pd nanoparticles with excellent electrocatalytic property on graphene oxide, J. Am. Chem. Soc. 133 (2011) 3693–3695.
[31] I.L. Alonso-Lemus, F.J. Rodriguez-Varela, M.Z. Figueroa-Torres, M.E. Sanchez-Castro, A. Hernandez-Ramirez, D. Lardizabal-Gutierrez, P. Quintana-Owen, Novel self-nitrogen-doped porous carbon from waste leather as highly active metal-free electrocatalyst for the ORR, Int. J. Hydrogen Energy 41 (2016) 23409–23426.
[32] A. Bharti, G. Cheruvally, Influence of various carbon nano-forms as supports for Pt catalyst on proton exchange membrane fuel cell performance, J. Power Sources 360 (2017) 196–205.
[33] Y. Liang, H. Wang, P. Diao, W. Chang, G. Hong, Y. Li, M. Gong, L. Xie, J. Zhou, J. Wang, T.Z. Regier, F. Wei, H. Dai, Oxygen reduction electrocatalyst based on strongly coupled cobalt oxide nanocrystals and carbon nanotubes, J. Am. Chem. Soc. 134 (2012) 15849–15857.
[34] Z. Sun, X. Wang, Z. Liu, H. Zhang, P. Yu, L. Mao, Pt-Ru/CeO_2/carbon nanotube nanocomposites: an efficient electrocatalyst for direct methanol fuel cells, Langmuir 26 (14) (2010) 12383–12389.
[35] C.R. Raj, A. Samanta, S.H. Noh, S. Mondal, T. Okajima, T. Ohsaka, Emerging new generation electrocatalysts for the oxygen reduction reaction, J. Mater. Chem. A 4 (2016) 11156–11178.
[36] S. Zhou, N. Liu, Z. Wang, J. Zhao, Nitrogen-doped graphene on transition metal substrates as efficient bifunctional catalysts for oxygen reduction and oxygen evolution reactions, ACS Appl. Mater. Interfaces 9 (2017) 22578–22587.
[37] D.H. Liu, H.Y. Lu, X.L. Wu, B.H. Hou, F. Wan, S.D. Bao, Q. Yan, H.M. Xie, R.S. Wang, Constructing the optimal conductive network in MnO-based nanohybrids as high-rate and long-life anode materials for lithium-ion batteries, J. Mater. Chem. A 3 (2015) 19738–19746.
[38] G. Sharma, P. Jeevanandam, Synthesis of self-assembled prismatic iron oxide nanoparticles by a novel thermal decomposition route, RSC Adv. 3 (2013) 189–200.
[39] Z.-I. Mohamed, H.-A. Muhammd, P. Lata, K. Kamlesh, Bulk and surface characteristics of pure and alkalized Mn_2O_3: TG, IR, XRD, XPS, specific adsorption and redox catalytic studies, New J. Chem. (1998) 875–882.
[40] J. Maryam, T. Satoshi, H. Joel, Phase pure α-Mn_2O_3 prisms and their bifunctional electrocatalytic activity in oxygen evolution and reduction reactions, Dalton Trans. 45 (2016) 18494–18501.
[41] H.-S. Jadhav, G.-M. Thorat, B.-B. Kale, J.-G. Seo, Mesoporous Mn_2O_3/reduced graphene oxide (rGO) composite with enhanced electrochemical performance for Li-ion battery, Dalton Trans. 46 (2017) 9777–9783.
[42] X. Yang, L.T. Roling, M. Vara, A.O. Elnabawy, M. Zhao, Z.D. Hood, S. Bao, M. Mavrikakis, Y. Xia, Synthesis and characterization of Pt–Ag alloy nanocages with enhanced activity and durability toward oxygen reduction, Nano Lett. 16 (2016) 6644–6649.
[43] M. Wang, J. Huang, M. Wang, D. Zhang, W. Zhang, Co_3O_4 nanorods decorated reduced grapheme oxide composite for oxygen reduction reaction in alkaline electrolyte, Electrochem. Commun. 34 (2013) 299–303.
[44] D.-H. Lim, J. Wilcox, Mechanisms of the oxygen reduction reaction on defective graphene-supported Pt nanoparticles from first-principles, J. Phys. Chem. C 116 (2012) 3653–3660.